

Day-Ahead Predictability of Complex Terrain Flows for Wind Resource Production: A Case Study of the Washoe Zephyr

CRAIG M. SMITH

Division of Atmospheric Sciences, Desert Research Institute, Reno, Nevada

DARKO KORAČIN

*Division of Atmospheric Sciences, Desert Research Institute, Reno, Nevada,
and University of Split, Split, Croatia*

KRISTIAN HORVATH

Meteorological and Hydrological Service, Zagreb, Croatia

(Manuscript received 21 February 2014, in final form 18 June 2014)

ABSTRACT

A detailed description of the meteorological conditions of the Washoe Valley (Nevada) and simulations that examine the predictability of the westerly high wind event known as the Washoe Zephyr are presented. Numerical weather model prediction skill is computed for day-ahead (24–48 h) forecasts of wind speed at a meteorological tower on the Virginia Hills range relative to a persistence forecast based on a seasonal climatology constructed of hourly mean observations. The model predictions are shown to be more skillful than a climatology based on seasonal and hourly means during winter and less skillful than the seasonal-hourly climatology (SHC) during summer. Overall skill of the forecasted winds tends to increase with finer horizontal grid spacing. Phase errors compose the largest component of the error decomposition and large phase errors are associated with the onset and decay of the diurnally forced Washoe Zephyr during summer and synoptically forced high wind events and valley rotors during winter. The correlation coefficient between forecasts and observations for all forecast horizontal grid spacings considered is shown to depend roughly linearly on the ratio of the integrated power spectral density in the synoptic band to the integrated power spectral density in the combined diurnal and subdiurnal band.

1. Introduction

Westerly high wind events, locally known as the Washoe Zephyr, are a common occurrence in the lee of the Sierra Nevada in northwestern Nevada. Commercial traffic on the main north–south transportation corridor (US-395) between Reno and the Nevada state capital, Carson City, is often subject to high wind restrictions that are triggered automatically by a Nevada Department of Transportation (NDOT) surface station on US-395 in the Washoe Valley. These high wind warnings, in which semi-truck traffic is prohibited, are issued by NDOT on average 10 times per month, and 30 high

profile trucks have crashed on US-395 due to high wind events since 1994. The current situation could potentially be exacerbated by the newly constructed 295-ft-high Galena Creek Bridge.

Washoe Zephyr high wind events are related to regional-scale pressure gradients between California's Central Valley and the elevated basin and range province in Nevada (Zhong et al. 2008), and, as we show later, downslope windstorms launched by nonlinear internal gravity waves (IGWs) in the immediate lee of the north–south-oriented Sierra Nevada. While high wind events farther to the south in California's Owens Valley have been the subject of intensive study (e.g., Grubišić et al. 2008), the zephyr in the Washoe Valley and the greater northwestern Nevada region has received much less consideration, despite the drastic effects that these events have on commercial shipping in the area.

Corresponding author address: Craig Smith, Division of Atmospheric Science, Desert Research Institute, 2215 Raggio Pkwy., Reno, NV 89512.
E-mail: craig.smith@dri.edu

During zephyr events, a persistent rotor is sometimes located in the eastern half of the Washoe Valley. Various mechanisms exist to explain this behavior. IGW breaking is often seen in numerical weather prediction (NWP) cross sections in northwestern Nevada (e.g., Cairns and Corey 2003), in southern Nevada (Pattantyus et al. 2011), and in the Owens Valley (Grubišić and Billings 2007). Spatial and temporal variability of high wind events and associated rotors has recently been noted in idealized modeling studies (Smith and Skillingstad 2009, 2011), observationally in the lee of the Sierra Nevada (Sheridan and Vosper 2012), and in the bora in coastal Croatia (Stiperski et al. 2012; Belušić et al. 2013). However, in general, accurate forecasting of the timing of downslope windstorms and the locations of rotor structures remains a difficult task for NWP models (Belušić et al. 2013). Additional considerations perhaps relevant for Washoe Valley high wind events include the extent to which the flow is modulated by the existence of a large gap in the Carson Range south of Mount Rose, and the influence of Lake Tahoe on the thermal structure of high wind events. Gap flow physics have been shown to be important in föhn events in the central Alps (Mayr et al. 2007), and lake effects on high wind events have been shown to be important to the Ora del Garda in the Italian Alps (Laiti et al. 2013).

To address shortcomings in wind energy prediction, the Desert Research Institute (DRI) and the National Renewable Energy Laboratory (NREL), alongside industry partners, have recently conducted wind resource assessment campaigns in the greater Nevada area (Belu and Koracin 2009), as well as in the Virginia Hills of Nevada, to elucidate details of topographically forced flows and enable evaluation of NWP models in complex terrain. While the previous meteorological tower campaign was used to examine the predictability of flows in complex terrain in general (Horvath et al. 2012), herein the latest field campaign including wind towers and sodar measurements is used to study the predictability of one specific meteorological phenomenon: the Washoe Zephyr and the associated Washoe Valley rotor circulation.

The goal of this paper is to examine the predictability of the Washoe Zephyr in the complex terrain of the Washoe Valley and Virginia Hills and explore, in detail, model forecast skill relative to this phenomena. The paper is structured as follows. An introduction to the local meteorological conditions and the field campaign is given in section 2. A description of the NWP model and our methodology is given in section 3. In section 4, we present a detailed computation and decomposition of the model's skill. An analysis of the forecast shortcomings is discussed in section 5. A summary and conclusions are given in section 6.

2. On the meteorology in the Washoe Valley

In the Washoe Valley and the greater region of northwestern Nevada (Fig. 1) there exist a number of surface stations that help elucidate meteorological phenomena of interest. NDOT maintains stations on the western side (WV-West) and center of the valley (WV-Center). The Citizen Weather Observer Program (CWOP) station on the eastern edge of the valley in New Washoe City appears to suffer from micrositing issues and, thus, is not included in this analysis. Additional stations of interest include the National Weather Service (NWS) and Federal Aviation Administration (FAA) stations at the Reno, Nevada (KRNO), and Sacramento, California (KSMF), airports; a DRI-maintained station on top of Slide Mountain (SLIDE); and a meteorological tower located on top of Mount Scott in the Virginia Hills range. All measurements from the meteorological tower are taken from the sensor at 60 m. The temporal resolution of the surface data as presented here is hourly, and that of the meteorological tower is 10 min. Details of these stations are given in Table 1.

Wind roses for the station in the center of the Washoe Valley along US-395 (WV-Center) and the 60-m sensor on the meteorological tower (Fig. 2) reveal a propensity for both of these stations to experience southwesterly and westerly high wind events. We define southwesterly high wind (SWHW) events as having wind speeds greater than 7 m s^{-1} and wind directions between 190° and 330° . We apply this definition to the 10-m wind from the surface stations and the 60-m sensor on the meteorological tower. Zephyr events are a subclass of SWHW events that typically occur during spring and summer afternoons and are regionally forced.

Contour plots (Fig. 3) in which single-year (meteorological tower) or multiyear (WV-Center) observations of wind speed are binned by hour of day and day of year show that, similar to other stations in the lee of the Sierra Nevada (Zhong et al. 2008), both WV-Center and the meteorological tower tend to experience higher wind speeds in the afternoon, especially during summer months. Similar plots of wind direction (not shown) reveal that these afternoon events tend to be associated with wind direction from the southwest. Overnight flows in the Washoe Valley are generally from the north and of low magnitude. The average afternoon wind speed at WV-Center is lower in winter than summer, suggesting a seasonal modulation of SWHW events in the Washoe Valley.

As suggested by the summer-only time series presented in Zhong et al. (2008, see their Fig. 5), we also find a strong relationship between regional-scale pressure

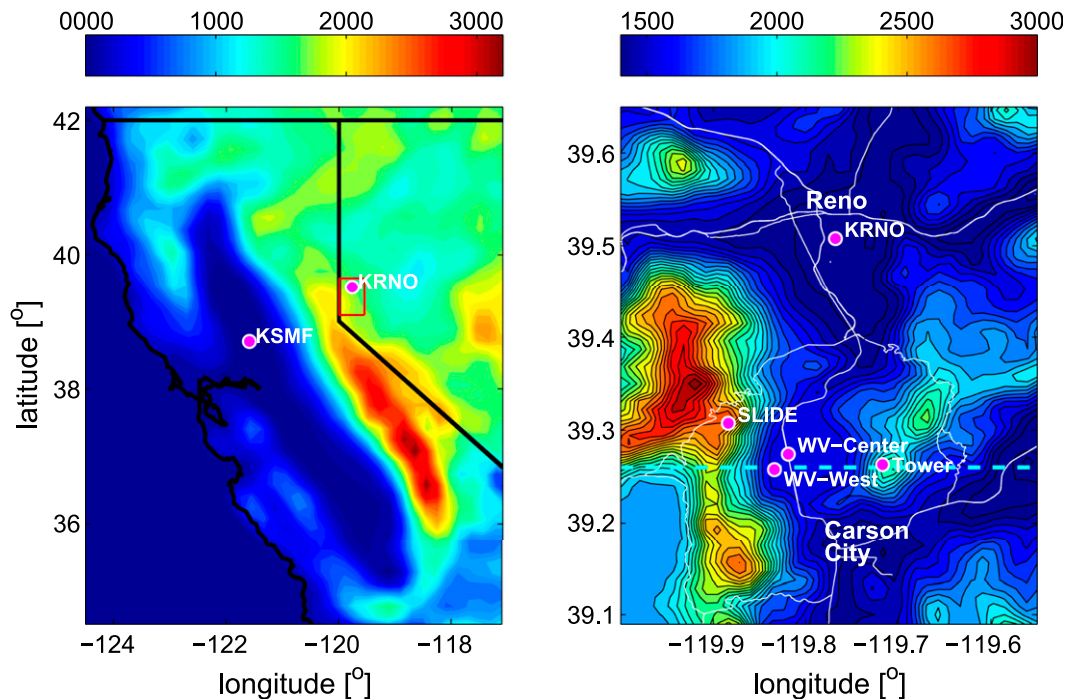


FIG. 1. (left) Topography (m) of California and northwestern Nevada and (right) close-up of the region of interest. Meteorological stations are indicated by the magenta circles, the region of interest is indicated by the red rectangle, major roads are indicated by white lines, and the locations of cross sections are indicated by the horizontal dashed cyan line. Sierra Nevada is the major mountain range running north–south (left). The northern extension of the Carson Range runs north–south. Lake Tahoe is in the lower left and the locations of Reno and Carson City are indicated. US-395 runs north–south and connects the two through the Washoe Valley. The Virginia Hills run southwest to northeast along the right side of the close-up view (right).

gradients (as measured by sea level pressure differences between Reno and Sacramento) and wind speed at WV-Center and the meteorological tower (Fig. 4) year-round. In contrast to the simpler relationship in the Columbia River Gorge (Sharp and Mass 2004; cf. Fig. 3), significant outliers to this relationship exist, for example, high wind speed and low or negative pressure difference, or low wind speed and high pressure difference. Some of the latter events might be due to the existence of strong and persistent cold air pools during wintertime (as measured by the potential temperature difference between the Slide Mountain station and KRNO), and some SWHW events might be generated or enhanced by local convection processes or mesoscale circulations nonaligned with

the Sacramento-to-Reno direction. Wintertime cold air pools in this area and elsewhere (Price et al. 2011; Dorninger et al. 2011; Sheridan et al. 2014) tend to be exacerbated by reflection of shortwave radiation by snow cover.

SWHW events tend to occur contemporaneously with positive easterly pressure gradients ($P_{\text{KSMF}} > P_{\text{KRNO}}$) and a lack of strongly stable stratification in the Washoe Valley—highly stable cases in the Washoe Valley are rarely subject to SWHW events, and SWHW events rarely occur in conjunction with strongly stable Washoe Valley inversions. The frequency of SWHW event occurrence as a function of pressure difference and valley inversion strength, normalized by the total occurrence

TABLE 1. Details of the surface stations and the meteorological tower, including station ID, location, beginning of period of record, and temporal resolution. The ending date for all data is 1 Nov 2013.

Station ID	Location	Lat (°N)	Lon (°W)	Elev (m)	Starting date	Resolution
KSMF	Sacramento, CA	38.701 39	121.593 89	60	1 Nov 2003	1 h
KRNO	Reno, NV	39.507 76	119.768 19	1342	1 Nov 2003	1 h
WV-West	Washoe Valley, NV	39.257 45	119.833 893	1539	1 Nov 2009	1 h
WV-Center	Washoe Valley, NV	39.273 81	119.818 81	1536	1 Nov 2003	1 h
SLIDE	Slide Mountain, NV	39.307 22	119.883 89	2941	1 Nov 2003	1 h
Tower	Virginia Hills, NV	39.262 80	119.716 94	2223	5 Oct 2012	10 min

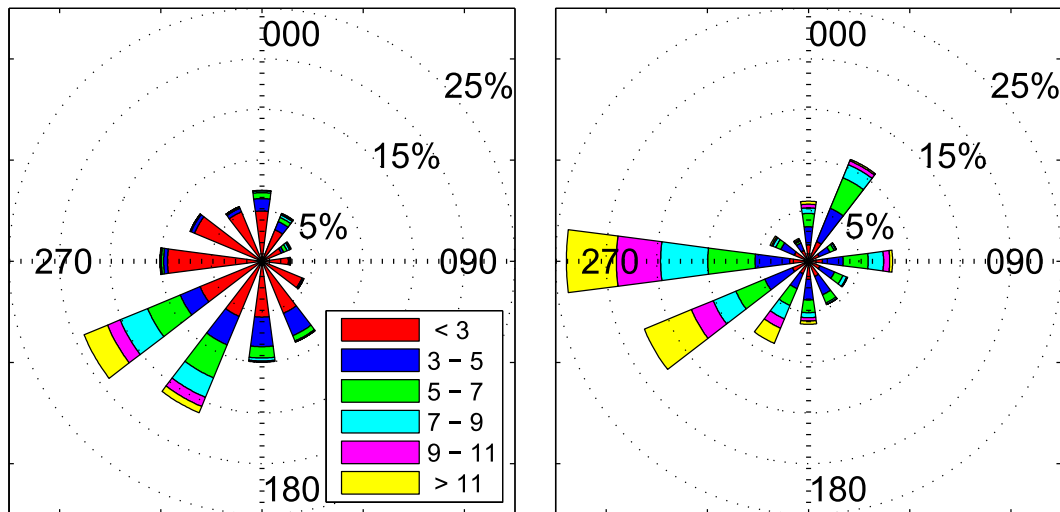


FIG. 2. Wind rose for the (left) WV-Center and (right) meteorological tower. Legend and color scheme indicate wind speed (m s^{-1}). Periods of record are 1 Nov 2003–1 Nov 2013 for WV-Center and 1 Nov 2012–1 Nov 2013 for the meteorological tower.

of any given combination of pressure difference and valley inversion strength (Fig. 5), shows that SWHW occurrence rates for high pressure difference and low static stability cases is very high, and SWHW occurrence for any given pressure bin is less likely in more stably stratified cases than less stably stratified cases.

Summertime (1 June–31 August) zephyr events in the western half of the Washoe Valley (WV-West and WV-Center) and on the meteorological tower tend to occur in the afternoon (Fig. 6), due to the diurnally varying regional pressure gradient, while high wind events in the wintertime (1 November–31 January) show no particular propensity for occurrence during any particular hour of day, as the mechanism for their formation is often synoptic-scale frontal passage.

Herein, we differentiate summertime (June–August) and wintertime (November–January) flows based on the substantially different forcing mechanisms that are evident in the amount of diurnal variability of the wind speed. Example time series of wind speed at the meteorological tower are shown in Fig. 7 for June 2013 and November 2012, which are representative of summertime and wintertime months, respectively. As can be seen in the time series, the summertime wind speed variability has a strong diurnal component, due to the zephyr and local topographically forced diurnal circulations, while the wintertime time series shows variability on much longer time scales—synoptic-scale frontal passage. Similar behavior has been noted for western-central Nevada where the share of diurnal variability (%) in total energy variance is around 10 times larger in summer than in winter (Horvath et al. 2012).

The mean diurnal cycle of vertical velocity (not shown) is also consistent with the importance of orographic lifting from the mean flow superimposed upon locally topographically forced circulations during summertime—hilltop katabatic divergence during evening and early morning ($w < 0$) and hilltop anabatic convergence ($w > 0$) during the afternoon.

Computation of the power spectral density PSD of the summertime and wintertime wind speed at the meteorological tower (Fig. 8) reveals quantitatively the extent to which the summertime flow is dominated by energy in the diurnal band, while the wintertime flow is dominated by energy in the synoptic band. A useful metric for elucidating details of the overall PSD is the ratio of integrated PSD in the synoptic band divided by the integrated PSD in the combined diurnal and subdiurnal bands r_{24} :

$$r_{24} = \frac{\int_{f(T=26\text{ h})}^{f(T=7\text{ days})} \text{PSD } df}{\int_{f(T=2\text{ h})}^{f(T=26\text{ h})} \text{PSD } df}, \quad (1)$$

where f is the frequency and T is the time period. As in Horvath et al. (2012), we also define the synoptic band to be time periods greater than 26 h, and the upper limit of the combined diurnal and subdiurnal band is 26 h. We chose to combine the diurnal and subdiurnal bands to allow for computation of one variable alone, which describes the phenomena of interest, and because of the portion of the diurnal variability that is aliased into the semidiurnal band. During summer the diurnal band

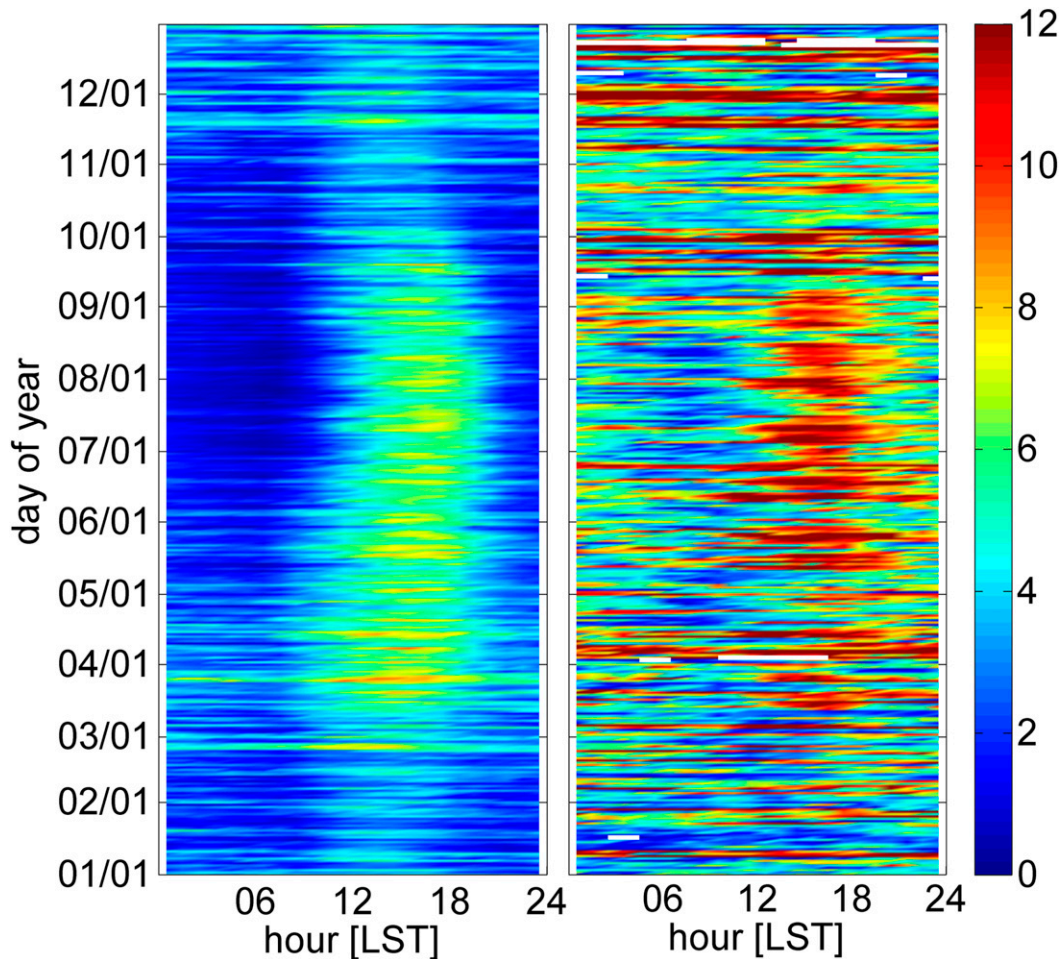


FIG. 3. Contour plot of wind speed (m s^{-1}) vs time of day and day of year for the (left) WV-Center and (right) meteorological tower. Periods of record are 1 Nov 2003–1 Nov 2013 for WV-Center and 1 Nov 2012–1 Nov 2013 for the meteorological tower.

comprises 83% of the combined diurnal and subdiurnal band, while in winter the diurnal band comprises 10% of the combined diurnal and subdiurnal band. Large values of r_{24} in wintertime indicate that the flow is dominated by energy in the synoptic band, and small values of r_{24} in summer indicate that the flow is instead dominated by energy in the diurnal and subdiurnal bands (Fig. 9). The variation of the magnitude of the monthly integrated PSD ratio (r_{24}) as a function of month of the field campaign forms the basis for our differentiation of results into summertime (1 June 2013–31 August 2013) and wintertime (1 November 2012–31 January 2013).

3. Model description and setup

Modeling experiments were performed with version 3.4.1 of the Weather Research and Forecasting (WRF) Model (Skamarock et al. 2008). Experiments were

initialized with Global Forecast System (GFS) boundary conditions at 6-h intervals and grid spacing of $0.5^\circ \times 0.5^\circ$. Since our interest was in day-ahead forecasts (24–48-h window), we allow the development of a full diurnal cycle and discard the first 24 h of each forecast as spinup. Each second-day forecast was accumulated for the calculation and analysis of the model skill over the entire period of the field campaign (1 October 2012–1 November 2013). Model output is saved every 10 min to match the temporal resolution of the meteorological towers' measurements. We used the following parameterizations in the WRF Model: Morrison's two-moment microphysics (Morrison et al. 2009), Rapid Radiative Transfer Model (RRTM) longwave radiation (Mlawer et al. 1997), the shortwave radiation scheme from Dudhia (1989), the Fifth-generation Pennsylvania State University–National Center for Atmospheric Research Mesoscale Model's (MM5) Monin–Obukhov similarity,

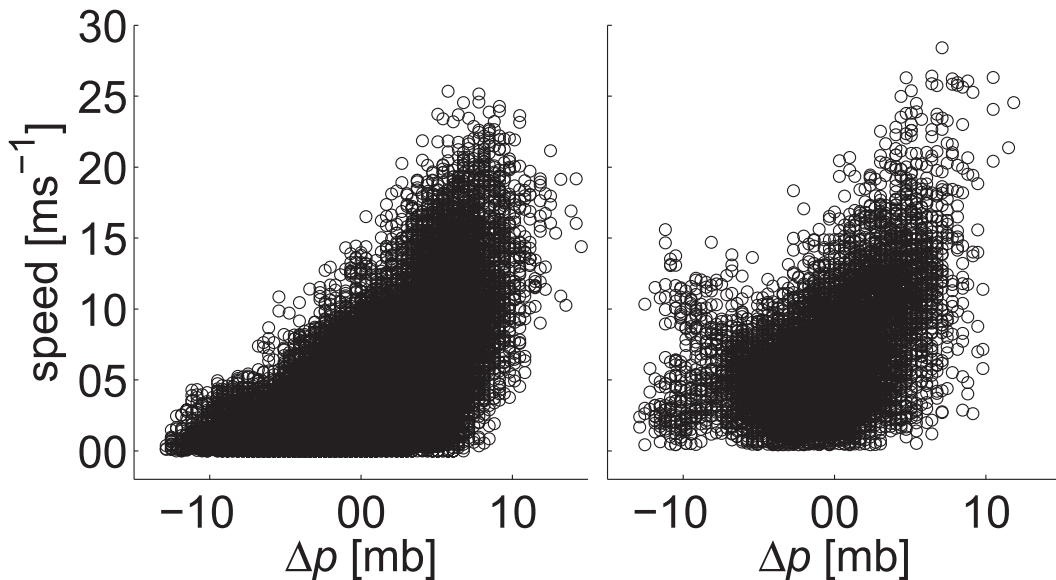


FIG. 4. Scatterplot of sea level pressure difference (KSMF – KRNO; mb) and wind speed (m s^{-1}) at the (left) WV-Center and (right) meteorological tower. Periods of record are 1 Nov 2003–1 Nov 2013 for WV-Center and 1 Nov 2012–1 Nov 2013 for the meteorological tower.

a unified Noah land surface model (Chen and Dudhia 2001), and Yonsei University's (YSU) nonlocal planetary boundary layer (PBL) scheme (Hong et al. 2006). The full years' worth of experiments were also completed with three other PBL parameterizations; however, results from their analysis were very similar those using the YSU scheme presented herein. We ran two separate WRF experiments with 47 vertical levels and one-way triple-nested domains configured with horizontal grid spacings of 18, 6, and 2 km, and 9, 3, and 1 km, respectively. The innermost domain was centered on the area of interest in northwestern Nevada (Fig. 1). The dimensions of the 1-km domain (2-km domain), roughly $100 \text{ km} \times 100 \text{ km}$ ($200 \text{ km} \times 200 \text{ km}$), were prescribed to avoid spurious numerical noise originating from the Davis relaxation coupling zone near the boundaries of nested domains. All results are presented in local standard time (LST = UTC – 8 h) and unless otherwise stated results are presented for the innermost domain only.

4. Decomposition of model skill

Computed PSD of each wind speed at the meteorological tower location from each WRF domain during summertime and wintertime reveal a significant deterioration of the model's ability to accurately capture the subdiurnal variability of flows for coarsely resolved domains (Fig. 10). In the high-frequency bands (greater than subdiurnal), the observed energy is significantly more than the modeled energy for coarse domains. In contrast, the domain with 2-km horizontal resolution

represents the roll off of PSD with increasing frequency in the subdiurnal range much better with respect to the observations. Presumably, this effect is largely due to a lack of accurate topographical representation in

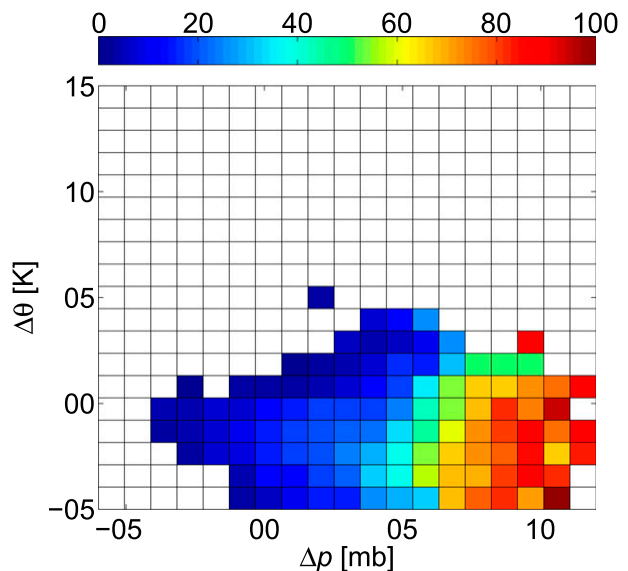


FIG. 5. Normalized frequency of SWHW event occurrence (%) (contoured) as a function of sea level pressure difference (KSMF – KRNO; mb) and the potential temperature difference in the Reno area (SLIDE – KRNO; K). Normalization is calculated as the number of SWHW occurrences per concurrent pressure difference bin and potential temperature bin divided by the total number of occurrences of concurrent pressure difference bin and potential temperature bin for all bins in which more than 500 cases exist. White space indicates bins for which there is an insufficient number of data points. Period of record is 1 Nov 2003–1 Nov 2013.

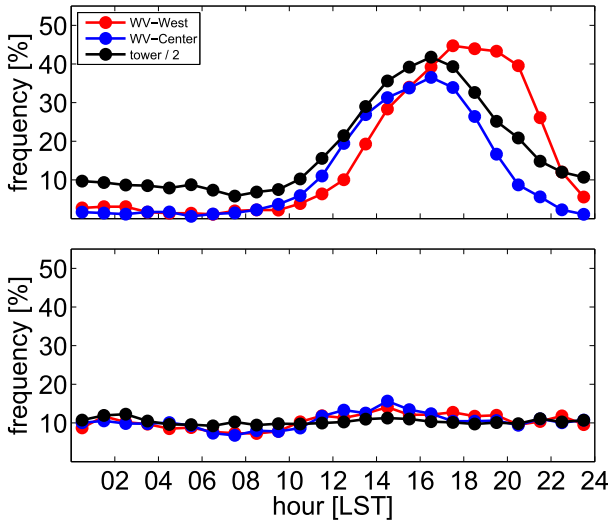


FIG. 6. Frequency of SWHW event occurrence during (top) summertime and (bottom) wintertime as a function of time of day for WV-West (red), WV-Center (blue), and the meteorological tower (black). For the sake of presentation, the frequency of SWHW occurrence at the meteorological tower has been divided by 2. Period of record is 1 Nov 2009–1 Nov 2013.

coarser domains. In the 18-km domain, the Virginia Hills range is essentially not present at all.

To assess the additional skill from the forecasts, we establish a baseline skill based on mean observations at the tower computed on an hourly basis during summertime and during wintertime. Model skill is computed relative to actual observations for the forecasts and for the climatological means computed on an hourly and seasonal basis, which hereafter are referred to as the seasonal-hourly climatology (SHC). The limited field

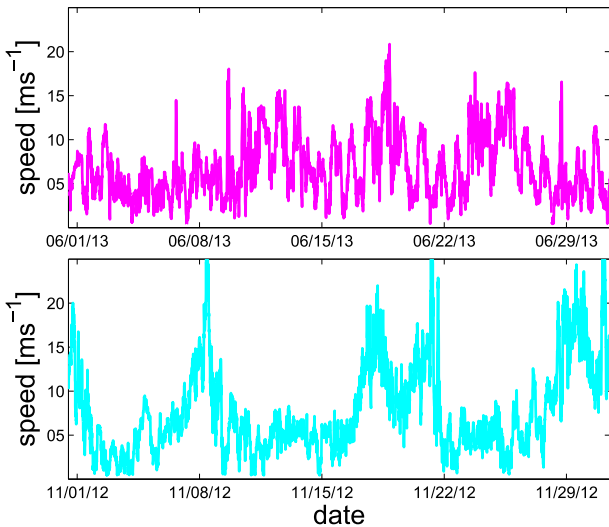


FIG. 7. Time series of wind speed (m s^{-1}) at the meteorological tower during (top) June 2013 and (bottom) November 2012.

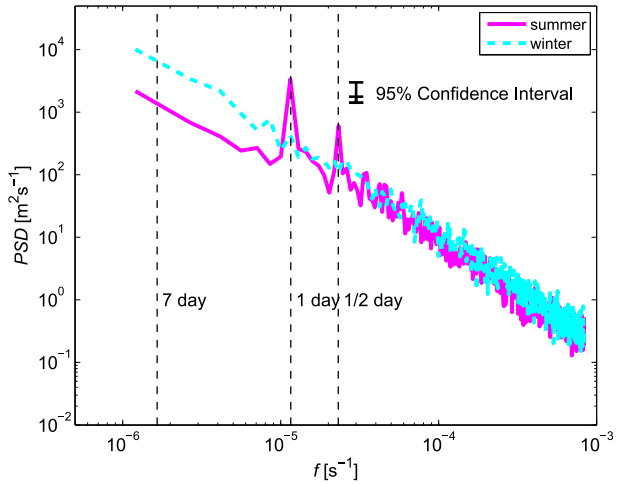


FIG. 8. PSD of wind speed from the meteorological tower as a function of frequency during summer (magenta) and winter (cyan). The vertical lines indicated periods corresponding to 7 days, 1 day, and $\frac{1}{2}$ day. The latter is useful for noting the aliasing of diurnal energy into a semidiurnal component. Black bars denote the 95% confidence interval.

campaign duration (~ 1 yr) precludes a construction of a more representative climatology, but this method nonetheless allows for computation of relative model skill. By definition, the bias of the SHC forecast is zero. We calculate bias as

$$\text{bias} = \frac{1}{n} \sum_{i=1}^n (v_{i,f} - v_{i,o}), \quad (2)$$

where v is the wind speed, f denotes the forecast (or SHC forecast), o denotes the observations, i denotes each individual 10-min period, and n denotes the total number of observations.

Mean observed and forecast horizontal wind speeds during wintertime show little diurnal variability (Fig. 11), while summertime observed and forecast mean horizontal wind speeds strongly depend on time of day, with a local maximum in the afternoon. All WRF domains during wintertime show a negative bias with respect to mean wind speed observations, but the bias is minimized in the finest-resolution domain. During

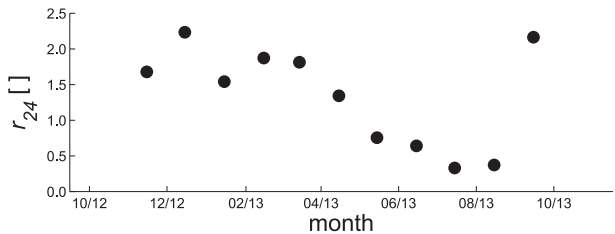


FIG. 9. Integrated monthly PSD ratio as a function of month of the field campaign.

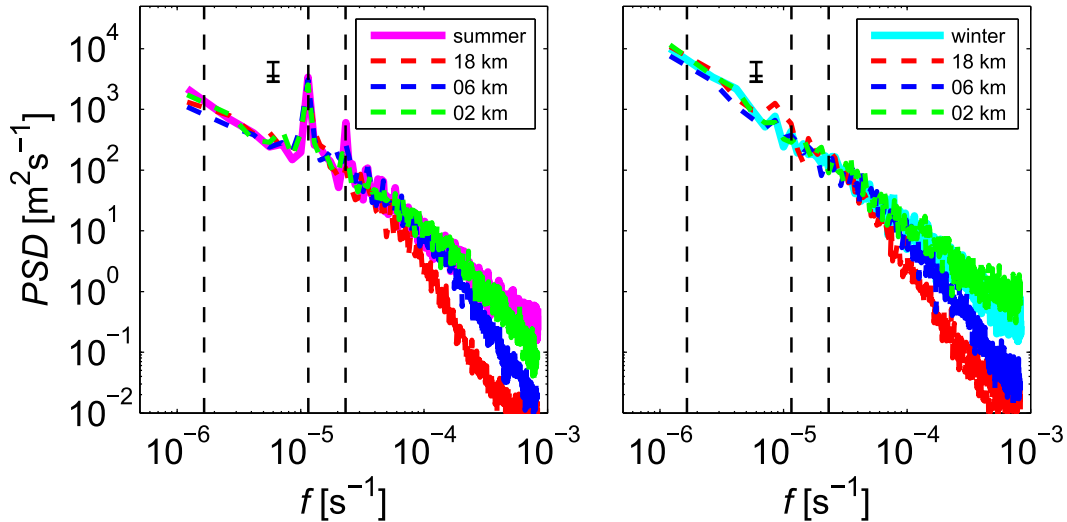


FIG. 10. PSD of wind speed from the meteorological tower during (left) summertime (magenta) and (right) wintertime (cyan) and computed from WRF Model domains with 18-km (red), 6-km (blue), and 2-km (green) horizontal resolution. The vertical lines, from left to right, indicated periods corresponding to 7 days, 1 day, and $1/2$ day. Black bars denote the 95% confidence interval.

summertime, bias is largest during the afternoon, with WRF generally underpredicting mean wind speed by close to 2 m s^{-1} .

We calculate RMSE as

$$\text{RMSE} = \sqrt{\frac{1}{n} \sum_{i=1}^n (v_{i,f} - v_{i,o})^2}. \quad (3)$$

In summer, all WRF domains underestimate wind speeds during the afternoon (Fig. 11), and the RMSE of the forecasts is also largest in the afternoon (Fig. 12). During summertime, the RMSE of the SHC is generally smaller than that of WRF throughout the day, while during wintertime the RMSE of the SHC is generally larger than the WRF predictions. During winter, WRF offers additional skill relative to the SHC. During summer, however, RMSE of all WRF domains increase greatly during afternoon (1200–1800 LST), while RMSE of the SHC increase relatively little during this time (Fig. 12). This relationship is indicative of errors associated with forecasting the magnitude and timing of the onset and decay of the zephyr. During summer, as indicated by the generally larger RMSE of all WRF domains relative to the SHC average, there is no additional skill in 24–48-h forecasts from WRF relative to SHC averages.

The additional skill relative to the SHC is calculated as

$$+\text{skill} = 100 \times \frac{(\text{RMSE}_f - \text{RMSE}_c)}{\text{RMSE}_c}, \quad (4)$$

where c denotes the climatology and is presented as a function of horizontal grid spacing for summertime and wintertime in Fig. 13. The most pronounced increase in skill is between 6- and 3-km horizontal resolution during summertime and wintertime. This result is qualitatively in accordance with the case studies presented in Cairns and Corey (2003). The increase in skill with respect to grid resolution is otherwise small. Overall, the relative additional skill in summertime is less than zero for all domains, indicating a poorer

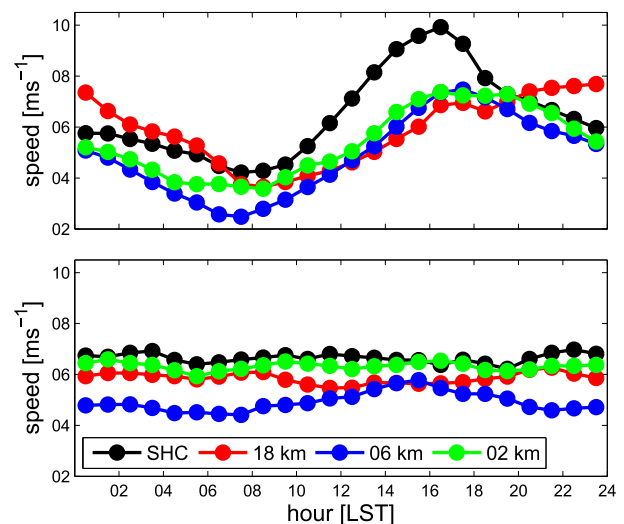


FIG. 11. Diurnal variation of mean hourly wind speed during (top) summer and (bottom) winter from SHC values (black) and WRF 18-km (red), 6-km (blue), and 2-km (green) domains.

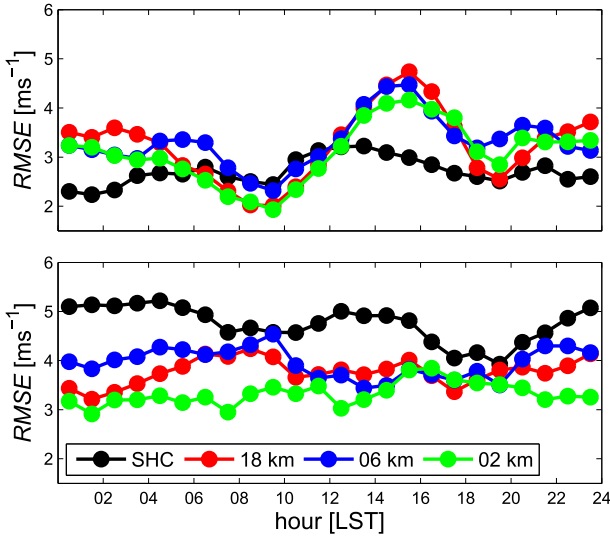


FIG. 12. As in Fig. 11, but for RMSE.

performance than using the SHC, with the caveat that our computed SHC by definition has zero bias.

Decomposition of the RMSE elucidates further details of model error. We follow the methodology suggested by Murphy (1988) and decompose the RMSE as

$$RMSE^2 = (\bar{v}_f - \bar{v}_o)^2 + (\sigma_f - \sigma_o)^2 + 2\sigma_o\sigma_f(1 - r_{fo}), \tag{5}$$

where the overbar denotes mean values, σ denotes the standard deviation, and r_{fo} denotes the linear correlation coefficient between the model forecast and observations. The terms on the right-hand side of Eq. (5) are presented in Fig. 14 and, from left to right, represent the square of the bias of the mean, the square of the bias of the standard deviation, and the square of the dispersion (phase) error, which is related to timing errors. The errors associated with the summer SHC and winter SHC, which do not depend on horizontal grid spacing, are presented as horizontal dashed lines in Fig. 14 to facilitate evaluation against the error of the forecasts. As noted before, the total RMSE of the wintertime SHC is larger than that of the WRF forecasts, which indicates the predictive skill in the forecasts, while the total RMSE of the summertime SHC is smaller than the forecasts, which indicates that the forecasts are less skillful overall than the SHC.

Phase error is the largest component in summertime and wintertime forecast decompositions. The mean of the bias error in the forecasts is generally the second largest term, and is zero by definition for the summer and winter SHC results. The bias of the standard deviation of the forecasts is the smallest decomposed term

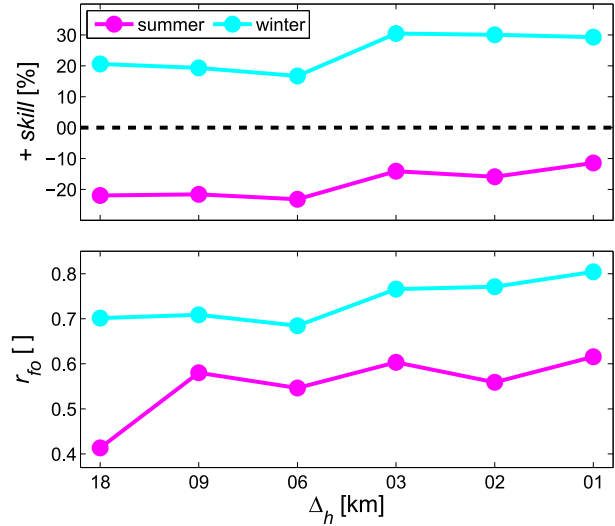


FIG. 13. (top) Normalized relative additional skill and (bottom) linear correlation coefficient as functions of grid spacing for wintertime (cyan) and summertime (magenta) forecasts (circles, solid line). The linear correlation coefficient in summertime is 0.53 and during wintertime it is 0.04.

during the summertime and wintertime forecasts. The bias of the standard deviation of the summer SHC is relatively small, while the bias of the standard deviation of the winter SHC is large due to the lack of diurnal variation in the mean hourly speed of the SHC, and the long tail distribution of the wind speed at the tower (not shown). Compared to summertime, the wintertime SHC has a broader distribution of wind speeds, and the WRF

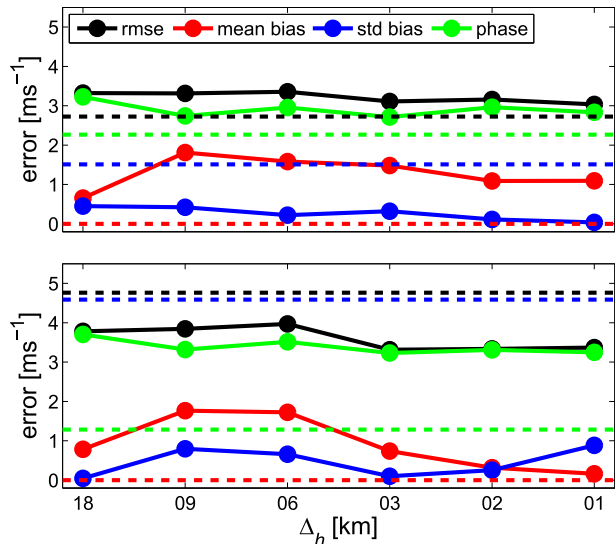


FIG. 14. RMSE (black) and RMSE decomposition terms of the bias of the mean (red), bias of the std dev (blue), and phase error (green) for the forecasts (circles, solid lines) as functions of the grid spacing and SHC (dashed lines) during (top) summertime and (bottom) wintertime.

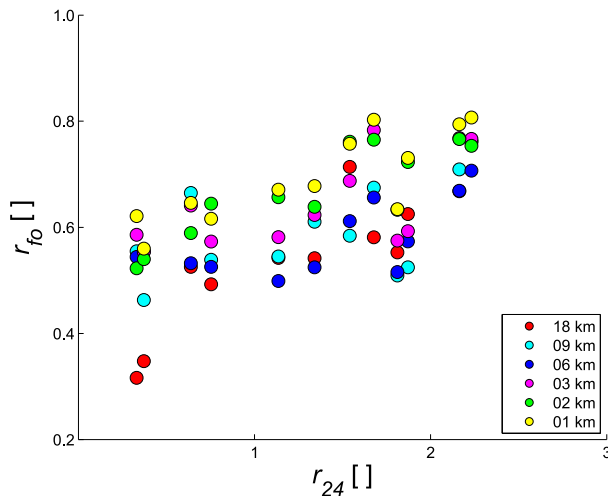


FIG. 15. Scatterplot of monthly linear dispersion coefficient of the forecasts plotted against the observed monthly integrated PSD ratio for the 18- (red), 9- (cyan), 6- (blue), 3- (magenta), 2- (green), and 1-km (yellow) WRF forecasts.

predictions and observations tend to be less distributed toward large magnitudes, which are particularly penalized by the RMSE metric.

An interesting anomaly is that of the decomposed error of the 18-km-resolution forecast skill. This domain exhibits relatively small mean bias error during summertime and wintertime, as well as relatively little error in the bias of the standard deviation during wintertime. We hypothesize that this inconsistency might be attributed to grid representativeness errors in the coarse topography of the 18-km run.

The relative importance of the decomposed phase error term in wintertime and summertime forecasts merits additional consideration. In Fig. 13 (bottom) we present the linear correlation coefficient, which is part of the phase (dispersion) error of the RMSE decomposition, between the observations and forecasts as a function of horizontal grid spacing. Wintertime forecasts generally show a secular, though not monotonic, increase in correlation coefficient with respect to increasing grid spacing, while in summertime there is relatively little change in correlation coefficient with respect to increasing grid resolution past 9 km. The linear correlation between the forecasts and observations is better in winter than summer. The summertime correlation of the forecast is higher than the SHC with the exception of the coarsest domain, and the winter correlation of the SHC is almost nil. An important overall point is the overall trend of increasing monthly computed correlation coefficient for all domains with increasing monthly PSD ratio (Fig. 15). In accordance with previous investigations (Rife et al. 2004), dispersion

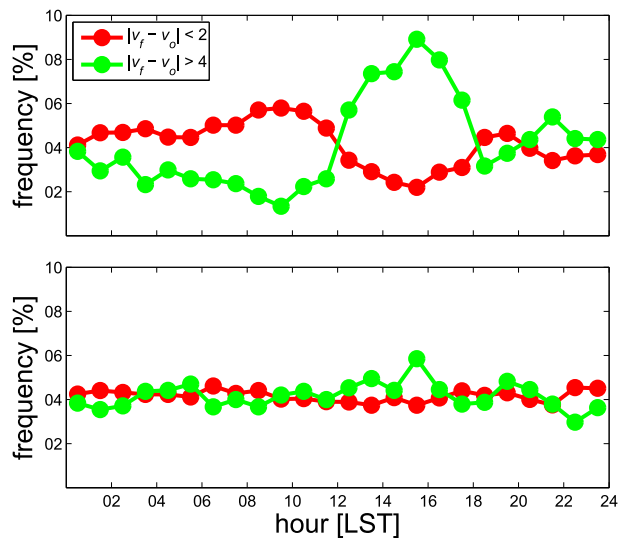


FIG. 16. Diurnal distribution of small (red) and large (green) errors in the 1-km-resolution run during (top) summer and (bottom) winter.

errors are less for cases in which synoptic-scale forcing is dominant relative to cases in which locally and regionally forced diurnal circulations are dominant for all forecast domains.

5. Discussion

Some insight into the nature of the phase errors associated with summertime forecasts can be gained through consideration of the diurnal variation of the magnitude of phase errors. We arbitrarily define small and large errors based on an absolute difference between forecast and observed wind speeds of less than 2 and greater than 4 m s^{-1} , respectively. Large errors associated with observations and forecasts during summertime exhibit a maximum during the afternoon (Fig. 16) and a minimum during the morning transition period. Small errors during summertime are at a minimum during the afternoon. In contrast, during the winter, small and large errors are evenly distributed throughout the day. Thus, large errors associated with both summertime and wintertime forecasts are consistent with phase errors associated with the onset, magnitude, and abatement of the summertime afternoon zephyr and wintertime synoptically forced SHW events (Figs. 6, 11, and 12).

Large phase errors in the wintertime forecasts tend to be associated with the launching of IGWs by synoptic-scale passage of the Sierra Nevada. An example cross section from the 1- and 6-km domains at 1100 LST 20 November and 0700 LST 21 November 2012 is presented in Fig. 17. A time series of wind direction and

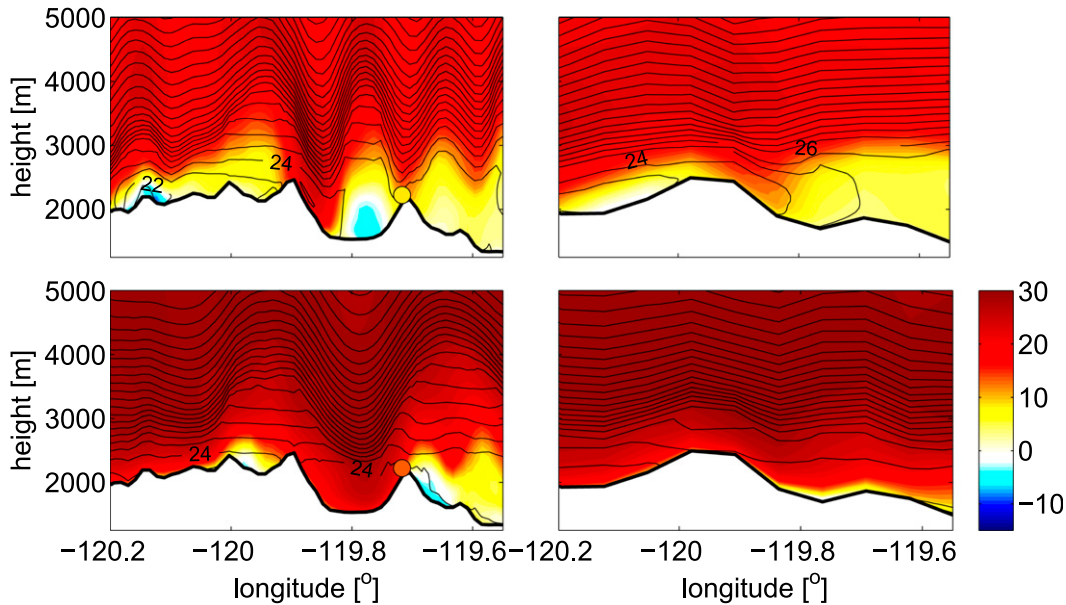


FIG. 17. Zonal component of velocity (filled; $m s^{-1}$) and isotherms (lines) along the cross section indicated in Fig. 1 from the (left) 1- and (right) 6-km-resolution runs at (top) 1100 LST 20 Nov and (bottom) 0700 LST 21 Nov 2012. The velocity at the tower is indicated by the circles in the 1-km domain.

wind speed during this event is shown in Fig. 18. The IGW activity associated with synoptic-scale passage in this area is highly transient, and the change in horizontal wavelength with time (Hills and Durran 2012), combined with the topography of the region, appear to determine the flow field. In the finescale simulation at 1100 LST 20 November, highly nonlinear IGWs are present over the Washoe Valley and a rotor spans the eastern half of the Washoe Valley. Note that the coarser (6-km resolution) model results completely miss the structure of the rotor and wave perturbations in the lower atmosphere. Lee-wave speedup is evident at the wind tower location. Later, at 0700 LST 21 November, a lee-wave pattern is present over the Washoe Valley that appears to interact constructively with the natural wavelength of the valley, and the flow extends far east, including the entire western slope of the Virginia Hills range. Wind speeds at the tower are very high. The 6-km domain, which is representative of all domains with coarser resolution in so far as the time series of wind speed does not correspond well to the observations and the topography of the Virginia Hills range is not well represented, does not exhibit the typical Washoe Valley rotor, and the IGWs over the crest of the Sierra Nevada are much smaller in amplitude and less nonlinear than those in the finely resolved domain. This result is in accordance with previous investigations (Grubišić and Stiperski 2009; Stiperski and Grubišić 2011). Essentially, the reduction in height of the Sierra Nevada, the reduction in height of the Virginia Hills range, and the decreasing steepness of

the leeside slope affects the model’s ability to generate nonlinear IGWs and maintain a persistent rotor nestled against the upstream flank of the secondary range.

We diagnose large phase errors associated with IGWs launched by the northern Carson extension via consideration of the largest absolute vertical velocity w_{IGW} above the Washoe Valley (longitude between 119.72° and $119.92^\circ W$ and altitude between 2800 and 4600 m).

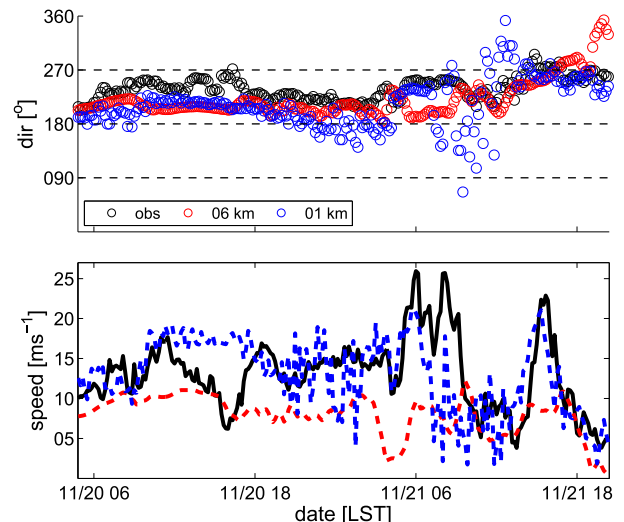


FIG. 18. Time series at the meteorological tower of (top) wind direction and (bottom) wind speed from the observations (black) and WRF 6-km (red) and 1-km (blue) domains during 20 and 21 Nov 2012.

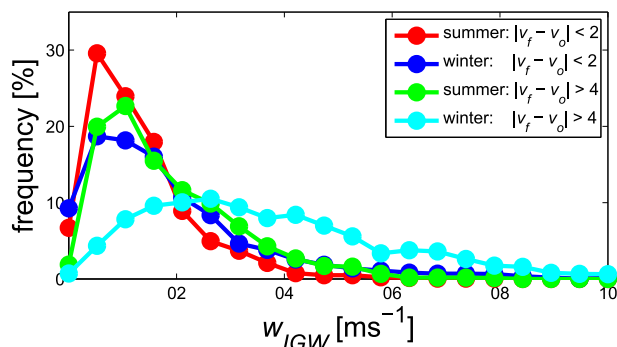


FIG. 19. Frequency of occurrence of maximum IGW vertical velocity associated with small errors during summer (red) and winter (blue), and large errors during summer (green) and winter (cyan).

During summertime, the distribution of w_{IGW} (Fig. 19) is relatively narrow and centered on low vertical wind speeds, indicating relatively small IGW activity over the Washoe Valley, and large phase errors are distributed similarly with respect to w_{IGW} as small phase errors. In contrast, wintertime large phase errors are much more likely to be associated with large w_{IGW} and nonlinear IGWs in the model predictions than wintertime small phase errors, indicating the importance and prominence of IGWs in problematic forecasting situations.

6. Conclusions

The focus of this study was on the relative model skill in predicting wind speed on the crest of the Virginia Hills in Nevada. A major phenomenon affecting flow at this site are southwesterly high wind events, which we segregated into summertime and wintertime types based on their forcing mechanism. During summertime, the onset and decay of the Washoe Zephyr is generally tied to diurnal forcing of the regional-scale pressure gradient, as measured by sea level pressure gradients between Reno and Sacramento, whereas, during wintertime, SWHW events were shown to occur more often in conjunction with IGW activity over the crest of the Sierra Nevada and in the Washoe Valley. Wind speeds of wintertime events tend to be higher than those of summer events, and they often occur contemporaneously with synoptic-scale frontal passage.

To examine the day-ahead (from 24 to 48 h) predictability of wind speed at the tower, we constructed a baseline persistence skill measure based on an SHC reference computed from hourly mean wind speeds averaged over summertime and wintertime months. Wintertime forecasts were overall more skillful than those of the SHC. The largest source of error in wintertime forecasts was in the phase (dispersion) term, and large phase

errors were more often associated with strong IGW activity in the model predictions than small phase errors. The two major sources of phase error during wintertime at this site are the timing and magnitude of SWHW events, along with the spatial structure/extent of the Washoe Valley rotor and its influence on wind speed over the secondary Virginia Hills range.

Summertime flow at the meteorological tower was marked by strong diurnal variability. Day-ahead forecasts during summertime were less skillful than those of the SHC, and the largest source of error during summer was also in the phase term. The majority of large summertime phase errors occurred in association with missed afternoon zephyr forecasts—onset, magnitude, and decay.

The forecasting experiment showed that the vertical structure and evolution of SWHW events can be revealed by a high horizontal grid spacing (1 km or higher). The flow field appears to be determined by the change in horizontal wavelength with time, which is adjusted with the topographic forcing. The simulations indicate highly nonlinear IGWs and occasional valley rotors in the eastern half of the Washoe Valley.

These results elucidate in detail the difficulties of forecasting wind resources in complex terrain. The meteorological phenomena specific to this site—locally and regionally forced diurnal circulations, trapped lee waves, rotors, and synoptic passage—are likely applicable to many existing and potential wind resource production areas in the mountainous American west and beyond. A clear relationship exists among the strength of the diurnal component of wind speed, phase error, and overall forecast skill for this location, and thus our work suggests the general utility of an overall paradigm based on the Murphy (1988) decomposition of model skill and considerations of the integrated power spectral density ratio of the wind speed that should be useful for other sites as well. Unlike bias corrections, phase errors cannot be minimized through the use of postprocessing of numerical weather prediction output using model output statistics (MOS). This research further suggests the primary importance of local meteorology that must be considered carefully for construction of numerical weather prediction frameworks in regions of complex terrain.

Acknowledgments. This research was funded by the Nell J. Redfield Foundation and the DOE–NREL under Grant NAX-9-66014-02 (DE-AC36-08G028308). KH is also supported by Grants EU-IPA2007/HR/161PO/001-040507 and MZOS 004-1193086-3036. We thank Jae Pullen of the Nevada Department of Transportation and David Myrick of the NWS Reno office for interesting

discussions of the Washoe Zephyr and its impact on the Washoe Valley.

REFERENCES

- Belu, R., and D. Koraćin, 2009: Wind characteristics and wind energy potential in western Nevada. *Renewable Energy*, **34**, 2246–2251, doi:10.1016/j.renene.2009.02.024.
- Belušić, D., M. Hrastinski, Ž. Večenjak, and B. Grisogono, 2013: Wind regimes associated with a mountain gap at the north-eastern Adriatic coast. *J. Appl. Meteor. Climatol.*, **52**, 2089–2105, doi:10.1175/JAMC-D-12-0306.1.
- Cairns, M., and J. Corey, 2003: Mesoscale model simulations of high-wind events in the complex terrain of western Nevada. *Wea. Forecasting*, **18**, 249–263, doi:10.1175/1520-0434(2003)018<0249:MMSOHE>2.0.CO;2.
- Chen, F., and J. Dudhia, 2001: Coupling an advanced land surface–hydrology model with the Penn State–NCAR MM5 modeling system. Part I: Model description and implementation. *Mon. Wea. Rev.*, **129**, 569–585, doi:10.1175/1520-0493(2001)129<0569:CAALSH>2.0.CO;2.
- Dorninger, M., C. D. Whiteman, B. Bica, S. Eisenbach, B. Pospichal, and R. Steinacker, 2011: Meteorological events affecting cold-air pools in a small basin. *J. Appl. Meteor. Climatol.*, **50**, 2223–2234, doi:10.1175/2011JAMC2681.1.
- Dudhia, J., 1989: Numerical study of convection observed during the Winter Monsoon Experiment using a mesoscale two-dimensional model. *J. Atmos. Sci.*, **46**, 3077–3107, doi:10.1175/1520-0469(1989)046<3077:NSOCOD>2.0.CO;2.
- Grubišić, V., and B. J. Billings, 2007: The intense lee-wave rotor event of Sierra Rotors IOP 8. *J. Atmos. Sci.*, **64**, 4178–4201, doi:10.1175/2006JAS2008.1.
- , and I. Stiperski, 2009: Lee-wave resonances over double bell-shaped obstacles. *J. Atmos. Sci.*, **66**, 1205–1228, doi:10.1175/2008JAS2885.1.
- , and Coauthors, 2008: The Terrain-Induced Rotor Experiment: A field campaign overview including observational highlights. *Bull. Amer. Meteor. Soc.*, **89**, 1513–1533, doi:10.1175/2008BAMS2487.1.
- Hills, M. O. G., and D. R. Durran, 2012: Nonstationary trapped lee waves generated by the passage of an isolated jet. *J. Atmos. Sci.*, **69**, 3040–3059, doi:10.1175/JAS-D-12-047.1.
- Hong, S.-Y., Y. Noh, and J. Dudhia, 2006: A new vertical diffusion package with an explicit treatment of entrainment processes. *Mon. Wea. Rev.*, **134**, 2318–2341, doi:10.1175/MWR3199.1.
- Horvath, K., D. Koraćin, R. Vellore, J. Jiang, and R. Belu, 2012: Sub-kilometer dynamical downscaling of near-surface winds in complex terrain using WRF and MM5 models. *J. Geophys. Res.*, **117**, D11111, doi:10.1029/2012JD017432.
- Laiti, L., D. Zardi, M. de Franceschi, and G. Rampanelli, 2013: Atmospheric boundary layer structures associated with the Ora del Garda wind in the Alps as revealed from airborne and surface measurements. *Atmos. Res.*, **132–133**, 473–489, doi:10.1016/j.atmosres.2013.07.006.
- Mayr, G. J., L. Armi, A. Gohm, D. R. Durran, C. Flamant, S. Gaberšek, A. Ross, and M. Weissmann, 2007: Gap flows: Results from the Mesoscale Alpine Programme. *Quart. J. Roy. Meteor. Soc.*, **133**, 881–896, doi:10.1002/qj.66.
- Mlawer, E. J., S. J. Taubman, P. D. Brown, M. J. Iacono, and S. A. Clough, 1997: Radiative transfer for inhomogeneous atmosphere: RRTM, a validated correlated-k model for the longwave. *J. Geophys. Res.*, **102**, 16 663–16 682, doi:10.1029/97JD00237.
- Morrison, H., G. Thompson, and V. Tatarskii, 2009: Impact of cloud microphysics on the development of trailing stratiform precipitation in a simulated squall line: Comparison of one- and two-moment schemes. *Mon. Wea. Rev.*, **137**, 991–1007, doi:10.1175/2008MWR2556.1.
- Murphy, A. H., 1988: Skill scores based on the mean square error and their relationships to the correlation coefficient. *Mon. Wea. Rev.*, **116**, 2417–2424, doi:10.1175/1520-0493(1988)116<2417:SSBOTM>2.0.CO;2.
- Pattantyus, A. K., S. Chiao, and S. Czyzyk, 2011: Improving high-resolution model forecasts of downslope winds in the Las Vegas valley. *J. Appl. Meteor. Climatol.*, **50**, 1324–1340, doi:10.1175/2011JAMC2586.1.
- Price, J. D., and Coauthors, 2011: COLPEX: Field and numerical studies over a region of Small Hills. *Bull. Amer. Meteor. Soc.*, **92**, 1636–1650, doi:10.1175/2011BAMS3032.1.
- Rife, D. L., C. A. Davis, and Y. Liu, 2004: Predictability of low-level winds by mesoscale meteorological models. *Mon. Wea. Rev.*, **132**, 2553–2569, doi:10.1175/MWR2801.1.
- Sharp, J., and C. F. Mass, 2004: Columbia Gorge gap winds: Their climatological influence and synoptic evolution. *Wea. Forecasting*, **19**, 970–992, doi:10.1175/826.1.
- Sheridan, P., and S. B. Vosper, 2012: High-resolution simulations of lee waves and downslope winds over the Sierra Nevada during T-REX IOP 6. *J. Appl. Meteor. Climatol.*, **51**, 1333–1352, doi:10.1175/JAMC-D-11-0207.1.
- , —, and A. R. Brown, 2014: Characteristics of cold pools observed in narrow valleys and dependence on external conditions. *Quart. J. Roy. Meteor. Soc.*, **140**, 715–728, doi:10.1002/qj.2159.
- Skamarock, W. C., and Coauthors, 2008: A description of the Advanced Research WRF version 3. NCAR Tech. Note, 113 pp. [Available online at http://www.mmm.ucar.edu/wrf/users/docs/arw_v3.pdf.]
- Smith, C. M., and E. D. Skillingstad, 2009: Investigation of upstream boundary layer influence on mountain wave breaking and lee wave rotors using a large eddy simulation. *J. Atmos. Sci.*, **66**, 3147–3164, doi:10.1175/2009JAS2949.1.
- , and —, 2011: Effect of inversion height and surface heat flux on downslope windstorms. *Mon. Wea. Rev.*, **139**, 3750–3764, doi:10.1175/2011MWR3619.1.
- Stiperski, I., and V. Grubišić, 2011: Trapped lee wave interference in the presence of surface friction. *J. Atmos. Sci.*, **68**, 918–936, doi:10.1175/2010JAS3495.1.
- , B. Ivančan-Picek, V. Grubišić, and V. Bajić, 2012: Complex bora flow in the lee of southern Velebit. *Quart. J. Roy. Meteor. Soc.*, **138**, 1490–1506, doi:10.1002/qj.1901.
- Zhong, S., J. Li, C. B. Clements, S. F. J. De Wekker, and X. Bian, 2008: Forcing mechanisms of the Washoe Zephyr—A daytime downslope wind system in the lee of the Sierra Nevada. *J. Appl. Meteor. Climatol.*, **47**, 339–350, doi:10.1175/2007JAMC1576.1.